

Article

A Self-Powered Broadband Photodetector with High Photocurrent Based on Ferroelectric Thin Film Using Energy Band Structure Design

Xing Gao, Xin Song, Shan Zhang, Xinxiang Yang, Pei Han, Liwen Zhang *, Chunxiao Lu *, Xihong Hao and Yong Li * 

Inner Mongolia Key Laboratory of Ferroelectric-Related New Energy Materials and Devices, School of Materials and Metallurgy, Inner Mongolia University of Science and Technology, Baotou 014010, China; gx15247821582@163.com (X.G.); 2019971@imust.edu.cn (X.S.); zhangs919@126.com (S.Z.); yxx199709112023@163.com (X.Y.); solidking@163.com (P.H.); xihonghao2022@163.com (X.H.)

* Correspondence: nkdlzw@imust.edu.cn (L.Z.); imustlxc@126.com (C.L.); liyong3062545@126.com (Y.L.)

Abstract: Self-powered photodetectors have the advantages of high sensitivity, sustainability, and small size and have become a research hotspot in advanced optoelectronic systems. However, the low output photocurrent density seriously hinders the practical application of ferroelectric self-powered photodetectors. Herein, the high-efficiency photoelectric detection performance of the $\text{Bi}_{1-x}\text{Ho}_x\text{FeO}_3$ ferroelectric self-powered photodetector is realized by doping Ho. The responsivity (R) and detectivity (D^*) can reach 0.0159 A/W and 1.94×10^{11} Jones under monochromatic light with a wavelength of 900 nm. Meanwhile, the R and D^* can reach 0.022 A/W and 2.65×10^{11} Jones under sunlight. These excellent photodetection performances are attributed to the high short-circuit current density (J_{sc}). When the Ho content is 6%, the output photocurrent reaches up to 0.81 mA/cm². The systematic structure and photo-electric characteristic analysis suggest that the decrease in the band gap leads to the generation of a larger photocurrent while the ferroelectric polarization is reduced slightly. This work provides a new way to obtain high-performance self-powered photodetectors.

Keywords: ferroelectric; thin-film; photodetector; self-powered; band gap



Citation: Gao, X.; Song, X.; Zhang, S.; Yang, X.; Han, P.; Zhang, L.; Lu, C.; Hao, X.; Li, Y. A Self-Powered Broadband Photodetector with High Photocurrent Based on Ferroelectric Thin Film Using Energy Band Structure Design. *Crystals* **2024**, *14*, 79. <https://doi.org/10.3390/cryst14010079>

Academic Editor: Serguei Petrovich Palto

Received: 30 November 2023

Revised: 6 January 2024

Accepted: 11 January 2024

Published: 13 January 2024



Copyright: © 2024 by the authors. Licensee MDPI, Basel, Switzerland. This article is an open access article distributed under the terms and conditions of the Creative Commons Attribution (CC BY) license (<https://creativecommons.org/licenses/by/4.0/>).

1. Introduction

Photodetectors have the ability to detect incident light or optical power and convert it into electrical signals, and they are widely used in communication, image sensing, optoelectronic information processing, medicine, environmental detection, and military fields [1–6]. Traditional photodetectors rely on an external power supply to realize their optical detection behavior. However, the external field generally leads to high dark current, a small switching ratio, large volume, and high energy consumption, which limits their practical applications [7–9]. Therefore, self-powered photodetectors that can operate without any external bias have effective application potential in future low energy consumption optoelectronics [10–12].

Among all the photodetectors, ferroelectric photodetectors have become a hotspot for their unique properties. Conventional photovoltaic semiconductor materials (p-n junction or metal-semiconductor) drive photogenerated carrier separation through a built-in electric field generated by the material, while ferroelectric photovoltaic materials are driven by the polarization electric field generated by their own inherent spontaneous polarization [13–18]. In addition, ferroelectric materials have a stable photocurrent, photovoltage above the band gap, small dark current, fast light response, and switchable photovoltaic output [19–22]. Recently, self-powered photodetectors based on ferroelectric materials, such as $\text{Pb}(\text{Zr,Ti})\text{O}_3$ (PZT) [23,24], BaTiO_3 (BTO) [25,26], and BiFeO_3 (BFO) [27,28], have been investigated. However, one of the greatest challenges for ferroelectric materials to date has been the low

photocurrent density, which limits the performance of photodetector. For instance, Gao et al. deposited BFO thin film on Pt/Ti/SiO₂/Si substrate using the sol-gel method and obtained J_{sc} of 105 $\mu\text{A}/\text{cm}^2$ under a 100 mW/cm^2 light intensity [29]. Gupta et al. prepared multiferroic (Ce, Mn) codoped BFO (BCFMO) thin films using the sol-gel method. Under the light intensity of 160 mW/cm^2 and the wavelength of 405 nm, they obtained a J_{sc} of 245 $\mu\text{A}/\text{cm}^2$ [30]. Inoue et al. prepared Mn-doped BTO single crystals and obtained a J_{sc} value of $\sim 35 \mu\text{A}/\text{cm}^2$ at a light intensity of 2.2 mW/cm^2 [31]. In fact, the photocurrent of ferroelectric materials is closely related to light absorption and photogenerated carrier separation [22,32]. The increase in ferroelectric polarization and the decrease in band gap are two important ways to improve photoelectric performance, which have been reported in many fields. Tian et al. found that Bi doping can enhance the ferroelectric properties of the BTO thin films without changing the band gap, thus improving the photocurrent and photoelectric detection performance [33]. Zhang et al. found that La doping can enhance residual polarization (P_r) of the PZT thin films, which improves the photocurrent [34]. Cai et al. showed that doped Ti at BFO thin films produced impurity energy levels, which reduced the band gap and increased the photocurrent density of the BFO thin films [35]. Among the conventional ferroelectric materials, like BTO, PZT, and BFO, BFO is the only single-phase material that has a low optical band gap (2.67 eV) and large remanent polarization. Hence, it is more appropriate for the fabrication of Vis–NIR self-powered photodetector [36]. In recent years, various photoelectric devices based on BFO have been investigated for their photoelectric response behaviors. For instance, Qi et al. designed a 4×4 matrix photodetector array based on BFO, which greatly improved the photoelectric detection performance [37]. Matsuo et al. report a “gap state” engineering method to enhance the photocurrent and produce an enormous photodetection performance [38]. Wang et al. constructed a mesoporous all-oxide architecture, with BFO as a photosensitizer and TiO₂ as a charge transport layer. This structure greatly promotes the extraction of photocarriers and achieves a high photovoltage [39]. These results indicate that BFO is the potential material in photoelectric fields. Because BFO has a markable residual polarization (P_r), it is relatively tricky to improve further, so it is an effective way to improve the photocurrent by adjusting the band gap. In this work, we achieve high-performance light detection by incorporating Ho elements in Bi sites of the BFO thin films, and the resulting thin film has a relatively small band gap. We investigated the effects of doping on the structure, ferroelectricity, bandgap, and photodetection performance of thin films.

2. Materials and Methods

2.1. Fabrication

In this study, $\text{Bi}_{1-x}\text{Ho}_x\text{FeO}_3/\text{La}_{0.7}\text{Sr}_{0.3}\text{MnO}_3$ (xBHFO/LSMO, $x = 0, 0.02, 0.04, 0.06, 0.08$) heterojunction was prepared at $1 \text{ cm} \times 1 \text{ cm}$ silicon base using sol-gel method. LSMO bottom electrode was fabricated by sol-gel method. A certain amount of manganese acetate (6157-78-1, Aladdin Industrial Corporation, Beijing, China), lanthanum acetate (257212-92-0, Aladdin Industrial Corporation, Beijing, China), and strontium acetate (543-94-2, Aladdin Industrial Corporation, Beijing, China) were added to the mixture of acetic acid and deionized water, and then acetylacetone was added. The molar concentration of the precursor solution was modulated to 0.1 mol/L by adding acetic acid. The precursor solution was heated at 80 °C for 2 h. A certain amount of bismuth nitrate [$\text{Bi}(\text{NO})_3 \cdot 5\text{H}_2\text{O}$] (10035-06-0, Aladdin Industrial Corporation, Beijing, China), ferric nitrate [$\text{Fe}(\text{NO})_3 \cdot 9\text{H}_2\text{O}$] (7782-61-8, Aladdin Industrial Corporation, Beijing, China), and holmium nitrate [$\text{Ho}(\text{NO})_3 \cdot 5\text{H}_2\text{O}$] (14483-18-2, Aladdin Industrial Corporation, Beijing, China) were dissolved in 2-methoxyethanol to obtain a xBHFO precursor solution. The molar concentration of the precursor solution was modulated to 0.2 mol/L by adding 2-methoxyethanol. The precursor solution was heated at 60 °C for 1 h. xBHFO and LSMO colloids were stirred at room temperature for 5 h and then aged for 24 h to obtain transparent colloids. The LSMO precursors were deposited on the Si substrates by using a spin coater with a spin speed of 1000 rpm for 3 s and then at 5000 rpm for 30 s. The LSMO wet film was pyrolyzed

at 150 °C and 400 °C and then annealed at 700 °C. The above heat treatment was repeated 5 times to obtain the LSMO film. The xBHFO ($x = 0, 0.02, 0.04, 0.06, 0.08$) precursors were deposited on the LSMO thin film by using a spin coater with a spin speed of 1000 rpm for 3 s and then at 3000 rpm for 30 s. The xBHFO wet film was pyrolyzed at 150 °C and 300 °C and then annealed at 550 °C. The above heat treatment was repeated 10 times to obtain xBHFO/LSMO heterojunction thin film. All the above annealing was carried out in an air atmosphere.

2.2. Device Preparation

In this work, the LSMO thin films simply conduct electricity. The LSMO colloid was prepared by sol-gel method. The LSMO colloid was deposited on Si substrate by spin-coated method to obtain LSMO wet film. The wet LSMO thin film was annealed to obtain LSMO/Si thin film. The $\text{Bi}_{1-x}\text{Ho}_x\text{FeO}_3$ (xBHFO) colloid was prepared by sol-gel method. The xBHFO wet film was obtained by depositing xBHFO on LSMO/Si thin film via spin-coating method. Using a wet cotton swab, the xBHFO wet film on the edge was wiped to expose the LSMO bottom electrode, and then the xBHFO/LSMO/Si film was obtained by annealing. Finally, Au electrodes with an area of 0.00196 cm^2 were deposited on the surface of xBHFO thin film using sputtering method to form Au/xBHFO/LSMO/Si photodetectors.

2.3. Characterization

The phase composition and structure of BFO film were analyzed by X-ray diffractometer (XRD, D8 Advance diffractometer, Bruker, Germany). The cross-section of BFO films was characterized by scanning electron microscopy (SEM, FEI Quanta 200, FEG, Beijing, China) to determine their stratification and thickness. The surface morphology of the films was analyzed by atomic force microscopy (AFM, Bruker, Icon, Emmingke, Tianjing, China). The domain structure of the thin films was analyzed by piezoelectric force microscopy (PFM, Bruker, Icon). The phase and amplitude of the film were analyzed by Kelvin probe microscope (KPFM, Bruker, Icon). Ferroelectric hysteresis loop (P-E) is measured by ferroelectric tester (Radiant Technologies, Inc., Albuquerque, NM, USA) at 2000 Hz. The photoelectric performance was measured by electrometer (2410, Keithley, Jianrong, Shanghai, China) and tunable color meter (TLS3-X75A-G, Zolix, NBeT, Beijing, China) under simulated sunlight source (100 mW/cm^2).

2.4. First Principle Methods

The calculations on density of states were performed using the CASTEP program code based on the first-principles plane-wave pseudo-potential method. The generalized gradient approximation (GGA) was adopted along with the exchange-correlation function realized by Perdow-Burke-Emzerhof (PBE). The plane wave cutoff energy of 500 eV and $2 \times 2 \times 2$ K-point Monkhorst-Pack grid were applied to guarantee a well-converged structure under study. A $2a \times 2b \times c$ supercell was adopted for all the calculations.

3. Results

Figure 1a shows the X-ray diffraction (XRD) patterns of the xBHFO thin films, which are deposited onto LSMO/Si substrates. All thin films possess a perovskite structure. Diffraction peaks of the BFO thin film can be assigned to a rhombohedral structure with an R3c space group. Figure 1b is the enlarged version of the XRD patterns in the vicinity of $2\theta = 32^\circ$. The (104) and (110) reflections are obviously separate in the pure BFO. With the increase in Ho content, the two split peaks (104)/(110) merge into one, indicating a change in phase structure. By analyzing the XRD pattern, it was found that the XRD diffraction pattern of the BFO thin film is consistent with the standard card PDF # 01-075-9475, indicating that the BFO thin film has the rhombohedral R3c structure. The XRD diffraction pattern of the 0.06BHFO thin film is consistent with the standard card PDF # 01-077-8894, indicating that the 0.06BHFO thin film has the orthorhombic Pbnm

structure. Therefore, Ho doping caused a structural transition of BFO thin films from the rhombohedral R3c structure toward the orthorhombic Pbnm structure. This transformation may result from the ionic radii difference between host ions ($\text{Bi}^{3+} \sim 1.17 \text{ \AA}$) and dopant ions ($\text{Ho}^{3+} \sim 1.015 \text{ \AA}$). Similar rare earth Ho-doped BFO also showed a corresponding structural transformation behavior [40].

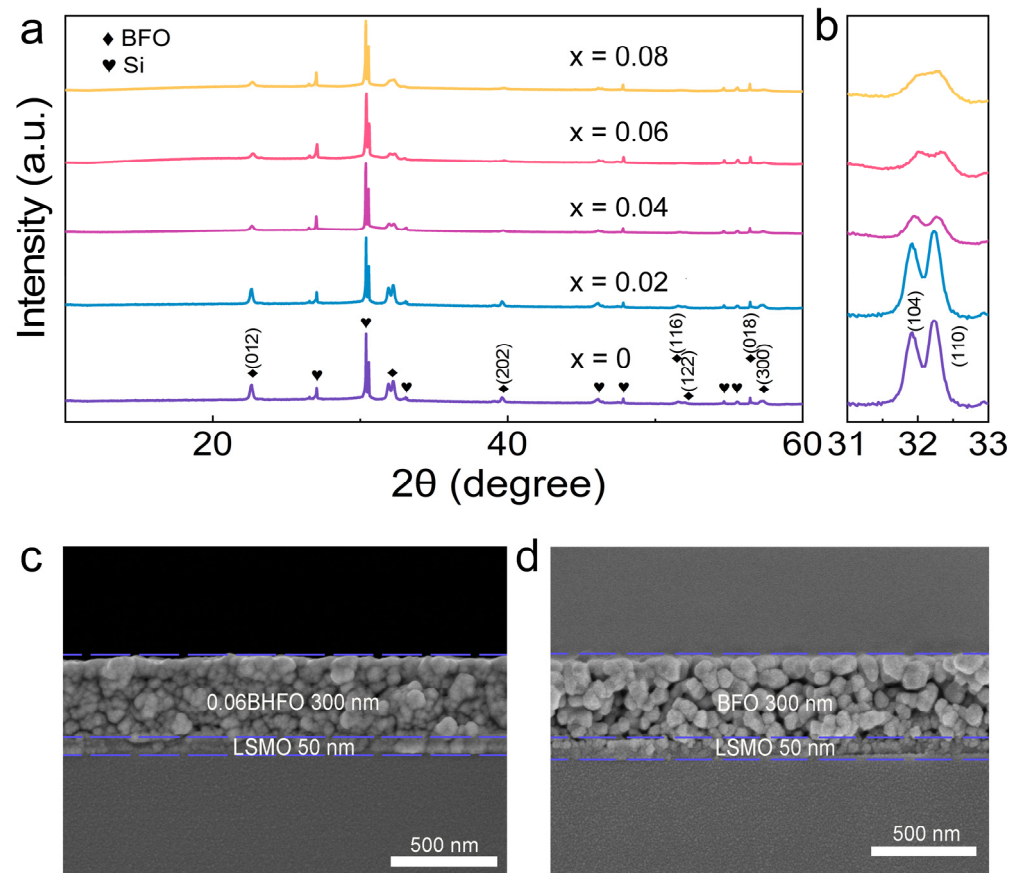


Figure 1. (a) XRD patterns of xBHFO thin films deposited on silicon substrate. (b) Enlarged XRD patterns of all the samples. (c) The SEM images of the 0.06BHFO/LSMO heterostructures and (d) The BFO/LSMO heterostructures.

The cross-sectional scanning electron microscope (SEM) images of the 0.06BHFO and the BFO thin films are shown in Figure 1c,d. The thickness of the BFO and the 0.06BHFO thin films is 300 nm, and the thickness of the LSMO film is 50 nm. With the increase in Ho content, the surface morphology of the thin film becomes smoother and denser. In addition, compared with the grain size of BFO thin film, 0.06BHFO thin film has smaller grain sizes. The reason for the decrease in grain size may be that the doping of Ho enhanced lattice strain energy and improved sintering quality [41,42].

The schematic of the photodetector in this work is presented in Figure 2a, where the area of the Au top electrode is 0.196 mm^2 . The Au/xBHFO/LSMO/Si device is electrically poled under +80 V at room temperature. Figure 2b,c show time-dependent short-circuit current (J_{sc}) and open-circuit voltage (V_{oc}) of the xBHFO thin films under the illumination of 100 mW/cm^2 . Obviously, the thin film exhibits a repeatable response to the light illumination, and the J_{sc} and V_{oc} have high stability. In addition, with the increase in Ho content, J_{sc} and V_{oc} present a change law of first increasing and then decreasing. Simultaneously, Figure 2d,e shows the variation of J_{sc} and V_{oc} with Ho content. J_{sc} and V_{oc} reach 0.81 mA/cm^2 and 0.052 V in the 0.06BHFO thin film, which are almost quadruple the J_{sc} and eightfold V_{oc} of the BFO thin film. Therefore, the doping of Ho improves the photovoltaic performances of the thin film. Figure 2f shows the external quantum efficiency

(EQE) of 0.06BHFO thin film at different wavelengths. EQE is one of the main performance indicators of photodetectors. Its value is the ratio of the number of collected electrons to the number of incident photons. As shown in Figure 2f, when the wavelength is 900 nm, the EQE value of 0.06 BHFO thin film is 1.61%. This indicates that light with a wavelength of 900 nm has a certain excitation effect on the 0.06BHFO thin film; therefore, the 0.06BHFO thin film will generate a certain photocurrent.

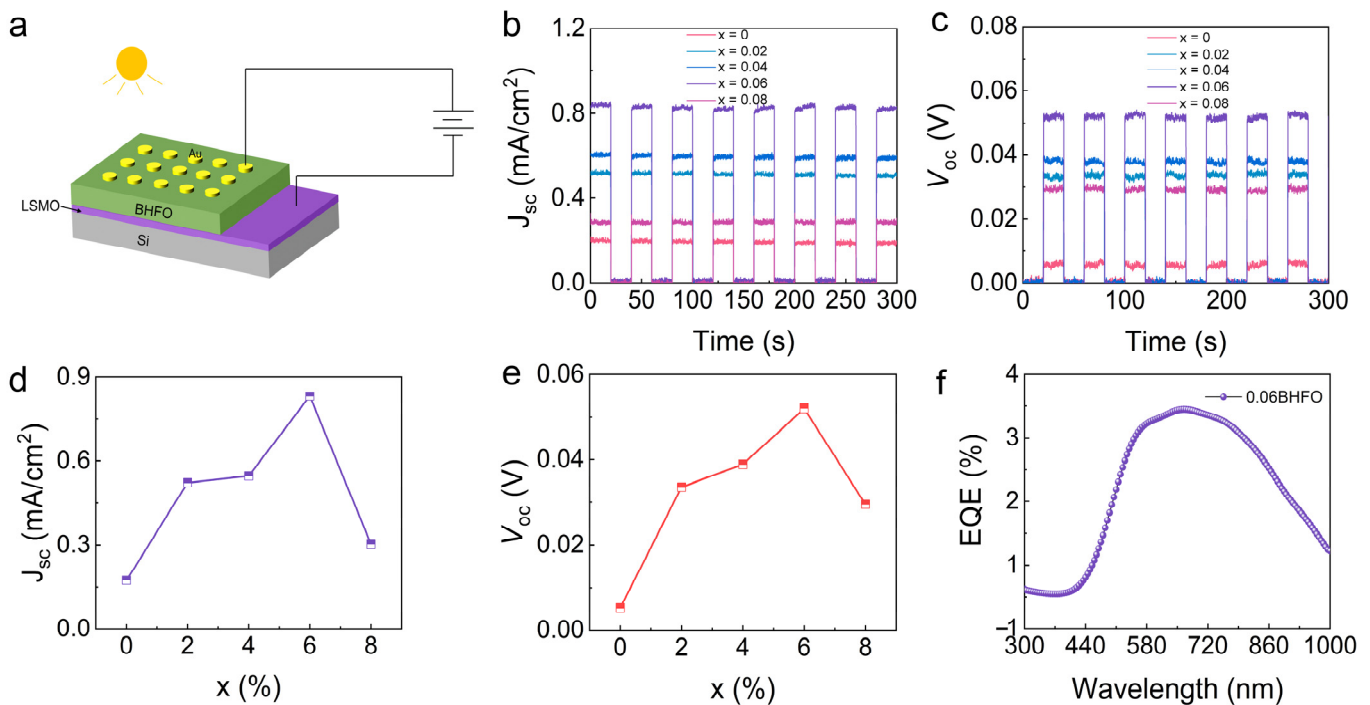


Figure 2. (a) Schematic illustration of the Au/xBHFO/LSMO/Si devices. Switching photovoltaic output of xBHFO thin films. Light ON/OFF cycles of (b) J_{sc} and (c) V_{oc} after poling with +80 V. The variation of (d) J_{sc} and (e) V_{oc} with Ho content. (f) External quantum efficiency (EQE) of 0.06BHFO thin film at different wavelengths.

To explore the origin of the enhanced photocurrent in the 0.06BHFO thin film, the properties related to the separation and transport of photogenerated carriers were investigated. Figure 3 shows the ferroelectric hysteresis loops of two thin films at 2000 Hz. The residual polarization (P_r) of the BFO thin film is 20.9 $\mu\text{C}/\text{cm}^2$, while the P_r of the 0.06BHFO thin film is 16.2 $\mu\text{C}/\text{cm}^2$. Obviously, with the increase in Ho content, the ferroelectric property decreases slightly, indicating that Ho doping at the BFO thin film causes a weak effect on the ferroelectric property. The reduction in ferroelectric property may be attributed to the fact that the smaller Ho ions cannot completely fill the blank space between the FeO_6 skeleton, resulting in a slight buckling between the ferric oxide octahedrons.

To further verify the ferroelectric result, AFM surface topography and PFM measurements were employed to analyze the domain structures of both thin films. The surface AFM of the BFO and 0.06BHFO thin films is shown in Figure 4a,d. Smooth and dense surface morphological features are observed in the BFO and 0.06BHFO thin films. Obviously, the grain size of the 0.06BHFO thin film is smaller than that of the BFO thin film, in agreement with the SEM result in Figure 1c,d. In addition, the grain and grain boundary could be distinguished clearly. Figure 4b,e show the OP PFM phase images of the BFO and 0.06BHFO thin films. Two thin films exhibit an obvious domain structure. Compared with the BFO thin film, the 0.06BHFO thin film has a smaller domain size, which may be attributed to the decrease in the degree of order in Ho doping. Figure 4c,f show the relationship between the OP phase and amplitude hysteresis loops of the BFO and 0.06BHFO thin films and the DC voltage. The BFO thin film has a saturated phase loop and a larger value of amplitude

than the 0.06BHFO thin film. These results imply that the BFO thin film possesses stronger ferroelectric polarization. Therefore, it can be concluded that the addition of Ho slightly reduces the ferroelectric polarization of the BFO thin film. However, the addition of Ho also reduces the size of domains and grains. In general, the ferroelectric polarization is not the reason for the change in the photovoltaic effect in the BFO thin film. Therefore, the band gap may be the dominant factor.

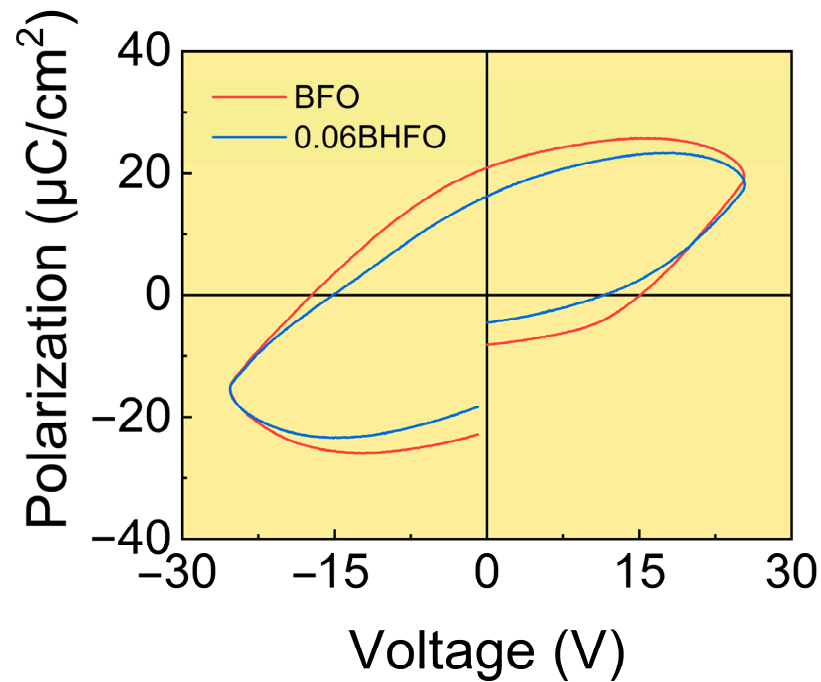


Figure 3. Ferroelectric hysteresis loops of the BFO and 0.06BHFO thin films at room temperature.

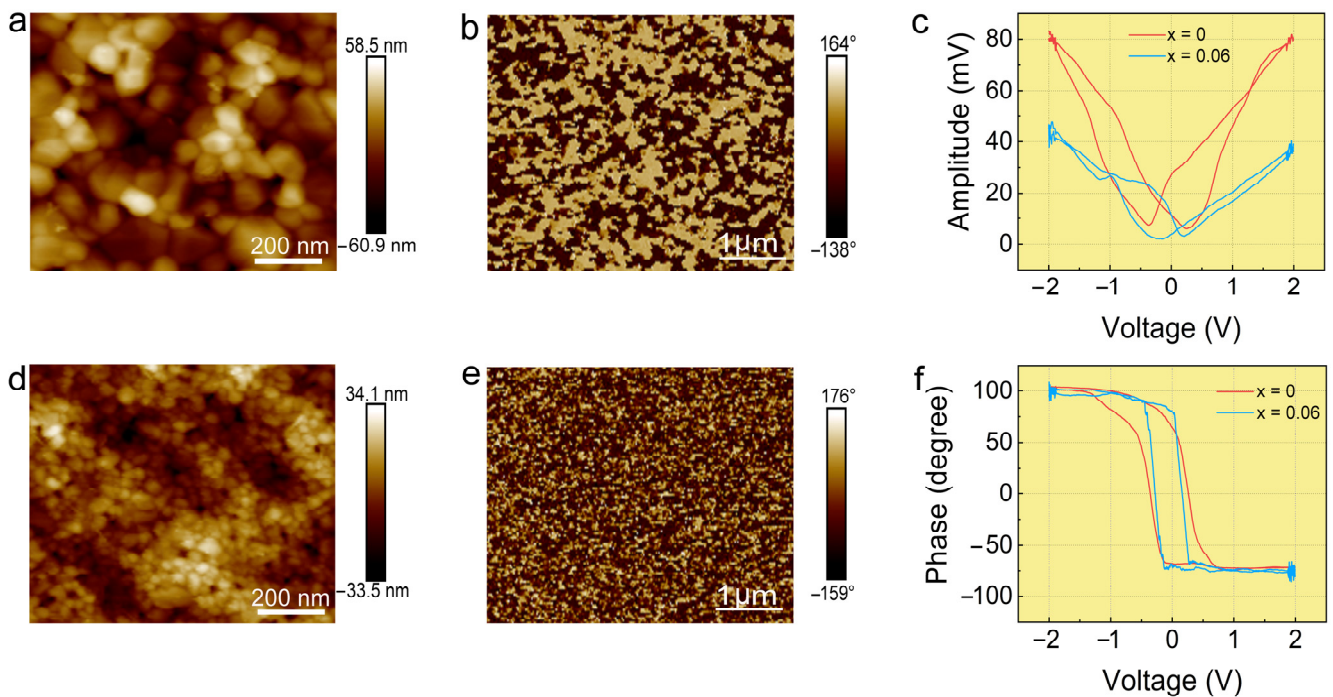


Figure 4. The AFM images of (a) the BFO thin film and (d) the 0.06BHFO thin film. Out-of-plane (OP) phase PFM images of (b) the BFO thin film and (e) the 0.06BHFO thin film. (c) Amplitude and (f) phase hysteresis loops of the BFO and 0.06BHFO thin films.

Figure 5a shows the UV-visible-NIR absorption spectra of the BFO and 0.06BHFO thin films. Obviously, the light absorption intensity of the 0.06BHFO thin film is higher than that of the BFO thin film. In addition, effective absorption is obtained in the infrared region, indicating that the thin films have the capacity to absorb a considerable amount of near-infrared light. In order to assess light absorption performance for the BFO and 0.06BHFO thin films under the experimental condition, the optical E_g of the BFO and 0.06BHFO thin films were estimated by using Tauc's Law, as in the following equation [43,44]:

$$(ah\nu)^2 = A(h\nu - E_g) \quad (1)$$

where a is the absorption coefficient of the measured sample, A is a constant related to the material, h is Planck constant, and ν is light frequency, respectively. Figure 5b shows the plot of $(ah\nu)^2$ as a function of $h\nu$ around the absorption edge for the BFO and 0.06BHFO thin films. The E_g of BFO thin film is about 2.4 eV, which is in agreement with the previous report [22]. With the increase in Ho content, the E_g is decreased, indicating that Ho doping at the Bi site of the BFO thin film causes a strong effect on the E_g . Moreover, an absorption peak appears in the 0.06BHFO thin film while the wavelength exceeds 850 nm (Figure 5c). It is found that the 0.06BHFO thin film also has an absorption edge of 1.27 eV, indicating that the 0.06BHFO thin film also has absorption in the near-infrared spectrum. Density functional theory (DFT) based on first principles indicates that the energy band of BFO and 0.06BHFO thin films are different. Figure 5d,e is the total orbital projected electron density of states for BFO and 0.06BHFO thin films. As shown in Figure 5e, a midgap state is created between the valence band and conductive band due to the strong interaction between Ho 4f and O s in 0.06BHFO. The midgap state enables the 0.06BHFO thin film to respond to the photons with lower energy (E1 and E2), as shown in Figure 5f. Particularly, the transition with the energy (E2) expands the photoresponse range to the near-infrared light band. Therefore, the energy band is the main reason for the variation of the photovoltaic effect in the 0.06BHFO thin film.

The 0.06BHFO thin film is a potentially Pb-free ferroelectric material with high photocurrent density and relatively low bandgap, which is highly expected to be applied as a self-powered photodetector. Hence, the photodetection performances of the 0.06BHFO were characterized systematically under sunlight. Figure 6a is the J_{sc} of Au/0.06BHFO/LSMO/Si device under illumination with various intensities under sunlight. The J_{sc} increases with enhancing illumination intensity, which exhibits obvious intensity-dependent characters. Response rate (R) and specific detectivity (D^*) are two critical parameters used to judge the performance of a photodetector. The R and D^* are calculated by the following equation [45,46]:

$$R = \frac{I_{on} - I_{off}}{P_{in}} \quad (2)$$

$$D^* = \frac{R}{\sqrt{2qI_{off}/S}} \quad (3)$$

where I_{on} is the photocurrent, I_{off} is the dark current, P_{in} is the light intensity, R is the response rate, q is the elementary charge, and S is the electrode area. Figure 6b shows R and D^* of the 0.06BHFO photodetector under illumination with various intensities under sunlight. The maximum R and D^* are 0.022 A/W and 2.65×10^{11} Jones under 10 mW/cm^2 . The response time refers to the time taken by the device to complete a photoelectric conversion process, and the response time is divided into rising time (τ_r , the time taken by the electrical signal from the peak value of 10% to 90%) and falling time (τ_d , the time taken by the electrical signal from the peak value of 90% to 10%). Figure 6c shows that the τ_r and τ_d of the 0.06BHFO photodetector are 0.6 ms and 9.5 ms, respectively. In addition, Figure 6d summarizes the comparison of the performances between the BFO and 0.06BHFO thin films. It is observed that the photodetection properties of the 0.06BHFO photodetector are superior to those of the BFO photodetector. Figure 6e shows the photocurrent diagram of 0.06BHFO thin film running under sunlight for 2000 s. Even in a long-running 2000 s

process, J_{sc} is almost constant, exhibiting high stability. The inset shows the J_{sc} -T diagram for the first 200 s of 0.06BHFO thin film. As shown in the inset, with the opening and closing of light, the 0.06BHFO thin film exhibits a spontaneous and repeatable response, indicating that the 0.06BHFO thin film exhibits switchable behavior. Moreover, the reliability of the device is further investigated. The J_{sc} does not degrade after aging at room temperature for more than 1 year (Figure 6f).

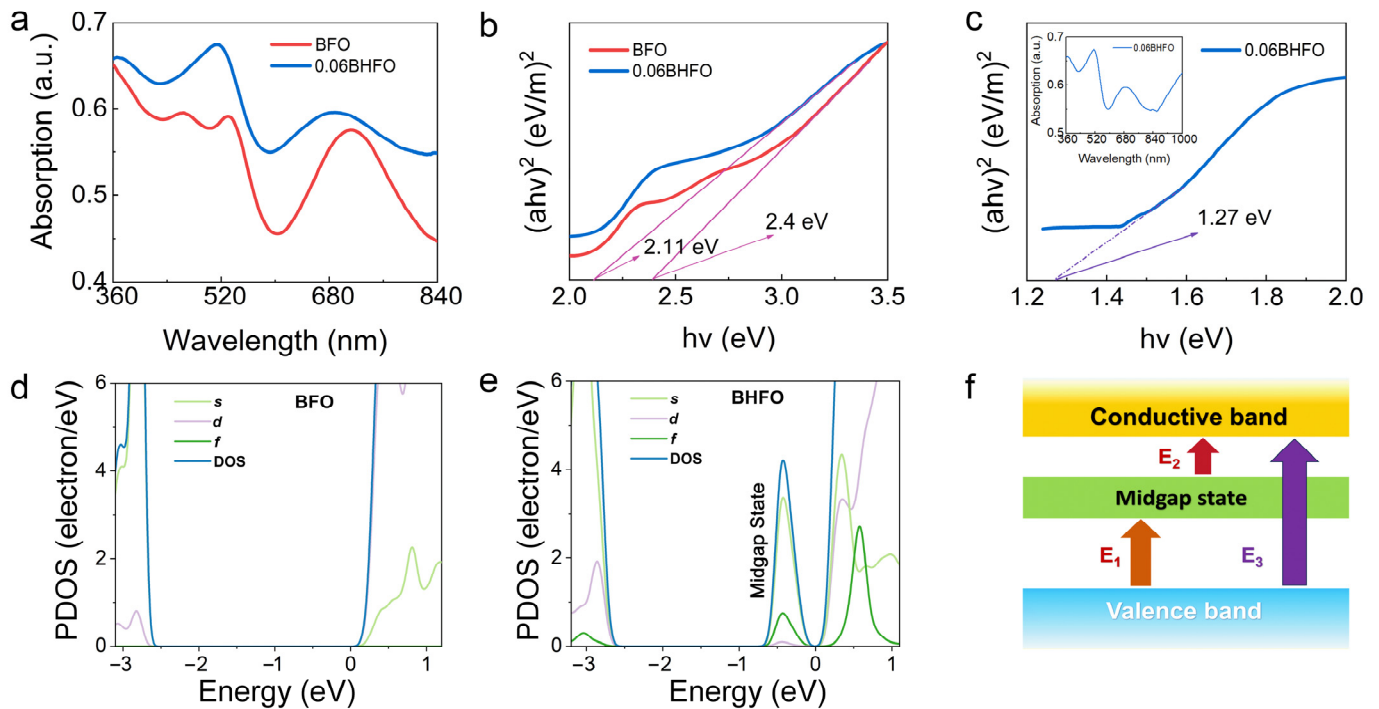


Figure 5. (a) The UV-Vis-NIR absorption spectra of the BFO and 0.06BHFO thin films. (b) The plot of $(ahv)^2$ as a function of $h\nu$ around the absorption edge for the BFO and 0.06BHFO thin films. (c) 0.06BHFO thin film in the range of 1.2–2 eV $(ahv)^2$ variation curve with $h\nu$. Total and orbital projected electronic density of state of the (d) BFO and (e) 0.06BHFO thin films. (f) Band structure model of 0.06BHFO thin film.

Figure 7a is the J_{sc} of the Au/0.06BHFO/LSMO/Si device with different illumination intensities under near-infrared light ($\lambda = 900$ nm). J_{sc} increases with enhancing illumination intensity. When the light intensity is $100 \mu\text{W}/\text{cm}^2$, the maximum J_{sc} is $1.18 \mu\text{A}/\text{cm}^2$. In addition, the maximum R and D^* are $0.0159 \text{ A}/\text{W}$ and 1.94×10^{11} Jones under near-infrared light, as shown in Figure 7b. Figure 7c shows the τ_r and τ_d of the 0.06BHFO photodetector in near-infrared light. The τ_r and τ_d are about 16.1 and 20.9 ms, indicating a fast near-infrared photodetector property. Figure 7d summarizes the performance comparison of the BFO and 0.06BHFO thin films at 900 nm. The results show that the photodetection performance of the 0.06BHFO photodetector is better than that of the BFO photodetector at a 900 nm wavelength. Table 1 summarizes the parameters of other self-powered photodetectors from the literature. It is worth noting that the R and D^* of the 0.06BHFO photodetector are several orders of magnitude larger than those of traditional perovskite ferroelectric photodetectors. Therefore, the 0.06BHFO-based self-powered photodetector, as a large polarization, narrow band gap, and high-efficiency photodetector, will have great application potential in optoelectronics.

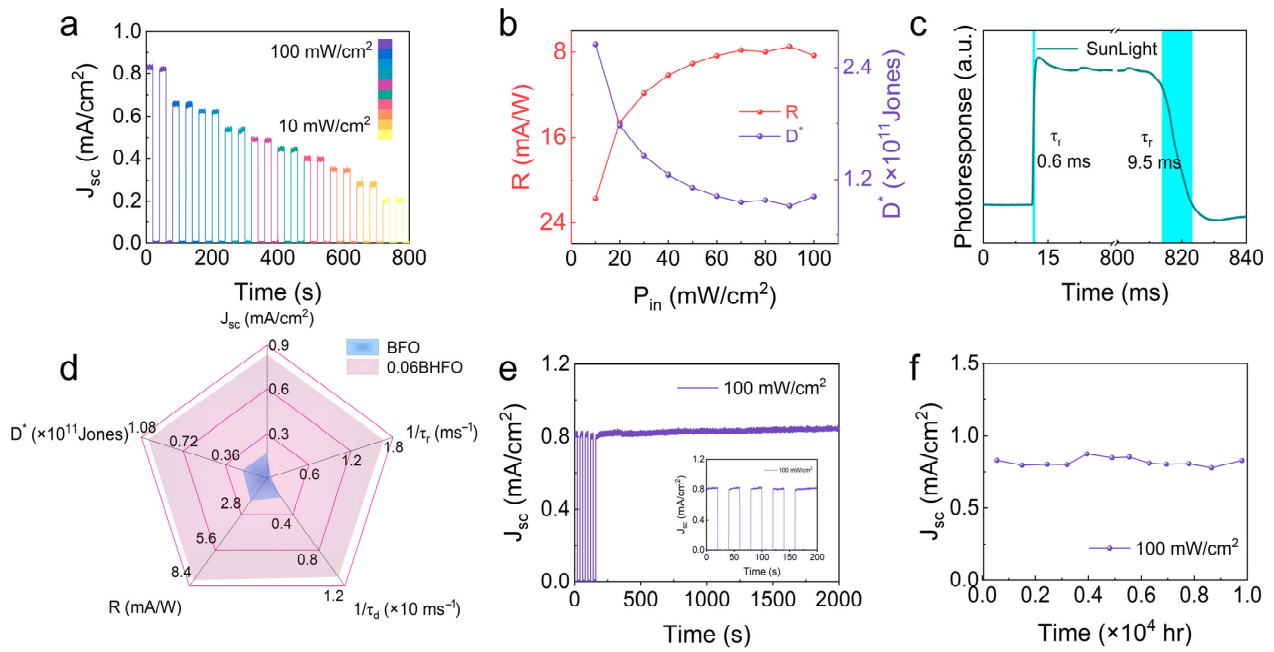


Figure 6. (a) Time-dependent J_{sc} of the 0.06BHFO photodetector under illumination with various intensities under sunlight. (b) R and D^* of the 0.06BHFO photodetector versus illumination intensity. (c) Response time of the 0.06BHFO photodetector. (d) The comparison of the photo-detection performances between the BFO and 0.06BHFO thin films under sunlight. (e) Photocurrent output stability of the 0.06BHFO thin film in a running process of 2000 s under illumination with sunlight. The inset shows the J_{sc} - T diagram for the first 200 s of 0.06 BHFO thin film. (f) J_{sc} value when the device ages more than one year.

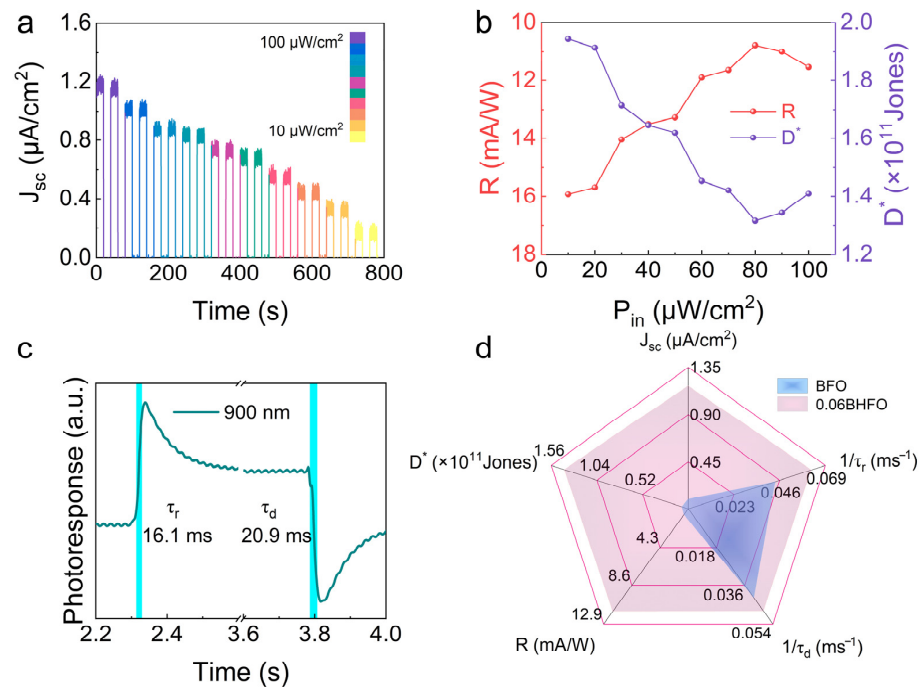


Figure 7. (a) Time-dependent J_{sc} of the 0.06BHFO photodetector under illumination with various intensities under 900 nm wavelength. (b) R and D^* of the 0.06BHFO photodetector versus illumination intensity under 900 nm wavelength. (c) Response time of the 0.06BHFO photodetector under illumination with the wavelength of 900 nm. (d) The comparison of the photo-detection performances between the BFO and 0.06BHFO thin films under illumination with the wavelength of 900 nm.

Table 1. The comparison of the performance of self-powered photodetector based on the various materials.

Photodetector	Light (nm)	τ_r (ms)	τ_d (ms)	Responsivity (A W ⁻¹)	Detectivity (Jones)	Ref.
Au/0.06BHFO/LSMO	sunlight	0.6	9.5	0.022	2.65×10^{11}	This work
Au/0.06BHFO/LSMO	900	16.1	20.9	0.0159	1.94×10^{11}	This work
Au/BLFO/LNO	sunlight	4.88	4.19	3.95×10^{-3}	5.05×10^9	[22]
FTO/BFO-TU/C	sunlight	4×10^3	4×10^3	2.85×10^{-6}	4.06×10^7	[47]
Au/BZT-BCT/Pt	sunlight	-	-	0.25	2.4×10^9	[48]
Pt/LFO/LNO/LAO	sunlight	15×10^{-3}	-	1×10^{-4}	10^8	[49]
BiFeO ₃ /NiO/RGO	sunlight	16.01	11.79	0.24×10^{-3}	3.67×10^{10}	[50]
ZnO/PbS	900	-	-	1.1×10^{-5}	7.2×10^7	[51]
MAPb _{0.5} Sn _{0.5} I ₃	900	-	-	0.514	1.49×10^{11}	[52]
FTO/BFCO/NiO/Ag	sunlight	0.23	0.38	9×10^{-6}	6.74×10^6	[53]

4. Conclusions

In summary, Au/xBHFO/LSMO/Si photodetectors with different holmium content were prepared using the sol-gel method. When the Ho content is 6%, the J_{sc} value is 0.81 mA/cm², practically four times that of BFO, and the V_{oc} value is 0.052 V, almost eight times that of BFO. A large output photocurrent will inevitably lead to high-sensitivity photoelectric detection. The Au/0.06BHFO/LSMO/Si photodetector has a maximum R and D^* of 0.022 A/W and 2.65×10^{11} Jones in single sunlight, respectively. Meanwhile, the maximum R and D^* are 0.0159 A/W and 1.94×10^{11} Jones in the near-infrared band (900 nm), respectively. Compared with pure Au/BFO/LSMO/Si devices, the performance of Au/0.06BHFO/LSMO/Si devices has been dramatically improved. The results show that high responsivity, significant detectivity, and fast response time from near-infrared were achieved in the BFO thin film photodetectors via Ho doping. This work provides a strategy for developing high-performance ferroelectric photodetectors.

Author Contributions: Conceptualization, X.G., X.S. and C.L.; methodology, X.G. and P.H.; validation, X.G., S.Z. and X.Y.; investigation, X.G.; resources, Y.L. and X.H.; data curation, X.G.; writing—original draft preparation, X.G.; writing—review and editing, Y.L., L.Z. and X.H.; Funding acquisition, Y.L. and X.H. All authors have read and agreed to the published version of the manuscript.

Funding: This work was supported by the Natural Science Foundation of China (12264036), the Natural Science Foundation of Inner Mongolia (2021JQ06), Basic Research Funds for Universities Directly under Inner Mongolia, Youth Science and Technology Talents Project of Inner Mongolia (NJYT22061), the Scientific and Technological Development Foundation of the Central Guidance Local (2021ZY0008), the Scientific research project of universities in Inner Mongolia (NJZZ23054), the “Light of the West” Talent Training Program of Chinese Academy of Sciences, the Program for “Grassland Talents” of Inner Mongolia, the Planning Project of Science and Technology of Ordos City (2022YY043), and the Talent Development Fund of Inner Mongolia.

Institutional Review Board Statement: Not applicable.

Informed Consent Statement: Not applicable.

Data Availability Statement: Data are contained within the article.

Acknowledgments: We would like to thank Xinxiang Yang and Shan Zhang for their help in drawing.

Conflicts of Interest: The authors declare no conflicts of interest.

References

- Konstantatos, G.; Howard, I.; Fischer, A.; Hoogland, S.; Clifford, J.; Klem, E.; Levina, L.; Sargent, E.H. Ultrasensitive solution-cast quantum dot photodetectors. *Nature* **2006**, *442*, 180–183. [\[CrossRef\]](#)
- Chen, G.; Yu, Y.; Zheng, K.; Ding, T.; Wang, W.; Jiang, Y.; Yang, Q. Fabrication of Ultrathin Bi₂S₃ Nanosheets for High-Performance, Flexible, Visible-NIR Photodetectors. *Small* **2015**, *11*, 2848–2855. [\[CrossRef\]](#)

3. Wu, D.; Jia, C.; Shi, F.; Zeng, L.; Lin, P.; Dong, L.; Shi, Z.; Tian, Y.; Li, X.; Jie, J. Mixed-dimensional PdSe₂/SiNWA heterostructure based photovoltaic detectors for self-driven, broadband photodetection, infrared imaging and humidity sensing. *J. Mater. Chem. A* **2020**, *8*, 3632–3642. [[CrossRef](#)]
4. Fang, H.; Xu, C.; Ding, J.; Li, Q.; Sun, J.-L.; Dai, J.-Y.; Ren, T.-L.; Yan, Q. Self-Powered Ultrabroadband Photodetector Monolithically Integrated on a PMN-PT Ferroelectric Single Crystal. *ACS Appl. Mater. Interfaces* **2016**, *8*, 32934–32939. [[CrossRef](#)]
5. Wu, D.; Guo, J.; Wang, C.; Ren, X.; Chen, Y.; Lin, P.; Zeng, L.; Shi, Z.; Li, X.J.; Shan, C.-X.; et al. Ultrabroadband and High-Detectivity Photodetector Based on WS₂/Ge Heterojunction through Defect Engineering and Interface Passivation. *ACS Nano* **2021**, *15*, 10119–10129. [[CrossRef](#)]
6. Wu, Y.L.; Fukuda, K.; Yokota, T.; Someya, T. A Highly Responsive Organic Image Sensor Based on a Two-Terminal Organic Photodetector with Photomultiplication. *Adv. Mater.* **2019**, *31*, 1903687. [[CrossRef](#)]
7. Wang, Y.; Fullon, R.; Acerce, M.; Petoukhoff, C.E.; Yang, J.; Chen, C.; Du, S.; Lai, S.K.; Lau, S.P.; Voiry, D.; et al. Solution-Processed MoS₂/Organolead Trihalide Perovskite Photodetectors. *Adv. Mater.* **2016**, *29*, 1603995. [[CrossRef](#)]
8. Cai, J.; Xu, X.; Su, L.; Yang, W.; Chen, H.; Zhang, Y.; Fang, X. Self-Powered n-SnO₂/p-CuZnS Core-Shell Microwire UV Photodetector with Optimized Performance. *Adv. Opt. Mater.* **2018**, *6*, 1800213. [[CrossRef](#)]
9. Li, Z.; Zhao, Y.; Li, W.; Peng, Y.; Zhao, W.; Wang, Z.; Shi, L.; Fei, W. A self-powered flexible UV-visible photodetector with high photosensitivity based on BiFeO₃/XTiO₃ (Sr, Zn, Pb) multilayer films. *J. Mater. Chem. A* **2022**, *10*, 8772–8783. [[CrossRef](#)]
10. Han, W.; Liu, K.; Yang, J.; Chen, X.; Ai, Q.; Zhu, Y.; Cheng, Z.; Li, B.; Liu, L.; Shen, D. High-performance self-powered amorphous-BaTiO₃/p-Si heterojunction photodetector controlled by ferroelectric effect. *Appl. Surf. Sci.* **2023**, *615*, 156371. [[CrossRef](#)]
11. Zhang, Q.; Xu, J.; Li, M.; Chen, J.; Xu, J.; Zheng, Q.; Shi, S.; Kong, L.; Zhang, X.; Li, L. High-performance self-powered ultraviolet photodetector based on BiOCl/TiO₂ heterojunctions: Carrier engineering of TiO₂. *Appl. Surf. Sci.* **2022**, *592*, 153350. [[CrossRef](#)]
12. Zhang, S.; Gong, A.; Yang, X.; Han, P.; Sun, N.; Li, Y.; Zhang, L.; Hao, X. Ultrahigh-performance self-powered photodetectors based on hexagonal YbMnO₃ ferroelectric thin films by the polarization-induced ripple effect. *Inorg. Chem. Front.* **2022**, *9*, 6448–6456. [[CrossRef](#)]
13. Chen, H.; Zhou, L.; Fang, Z.; Wang, S.; Yang, T.; Zhu, L.; Hou, X.; Wang, H.; Wang, Z.L. Piezoelectric Nanogenerator Based on In Situ Growth All-Inorganic CsPbBr₃ Perovskite Nanocrystals in PVDF Fibers with Long-Term Stability. *Adv. Funct. Mater.* **2021**, *31*, 2011073. [[CrossRef](#)]
14. Yu, R.; Pan, C.; Chen, J.; Zhu, G.; Wang, Z.L. Enhanced Performance of a ZnO Nanowire-Based Self-Powered Glucose Sensor by Piezotronic Effect. *Adv. Funct. Mater.* **2013**, *23*, 5868–5874. [[CrossRef](#)]
15. Wang, X.; Wang, P.; Wang, J.; Hu, W.; Zhou, X.; Guo, N.; Huang, H.; Sun, S.; Shen, H.; Lin, T.; et al. Ultrasensitive and Broadband MoS₂ Photodetector Driven by Ferroelectrics. *Adv. Mater.* **2015**, *27*, 6575–6581. [[CrossRef](#)] [[PubMed](#)]
16. Jin, H.J.; Park, C.; Lee, K.J.; Shin, G.H.; Choi, S.Y. Ultrasensitive WSe₂/α-In₂Se₃ NIR Photodetector Based on Ferroelectric Gating Effect. *Adv. Mater. Technol.* **2021**, *6*, 2100494. [[CrossRef](#)]
17. Butler, K.T.; Frost, J.M.; Walsh, A. Ferroelectric materials for solar energy conversion: Photoferroics revisited. *Energy Environ. Sci.* **2015**, *8*, 838–848. [[CrossRef](#)]
18. Gong, A.; Zhang, S.; Li, Y.; Han, P.; Lu, C.; Sun, N.; Zhao, Y.; Xing, L.; Zhang, L.; Hao, X. Broadband, high-sensitivity self-powered ferroelectric LuMnO₃-based photodetector with large photocurrent output. *Ceram. Int.* **2023**, *49*, 12462–12468. [[CrossRef](#)]
19. Yuan, Y.; Xiao, Z.; Yang, B.; Huang, J. Arising applications of ferroelectric materials in photovoltaic devices. *J. Mater. Chem. A* **2014**, *2*, 6027–6041. [[CrossRef](#)]
20. Zhang, J.; Xue, W.; Chen, X.-Y.; Hou, Z.-L. Sm doped BiFeO₃ nanofibers for improved photovoltaic devices. *Chin. J. Phys.* **2020**, *66*, 301–306. [[CrossRef](#)]
21. Liu, X.; Zhang, F.; Long, P.; Lu, T.; Zeng, H.; Liu, Y.; Withers, R.L.; Li, Y.; Yi, Z. Anomalous Photovoltaic Effect in Centrosymmetric Ferroelastic BiVO₄. *Adv. Mater.* **2018**, *30*, 1801619. [[CrossRef](#)]
22. Wang, G.; Gong, A.; Zhang, S.; Tian, M.; Liu, J.; Li, Y.; Hao, X. High performance self-powered photodetector based on ferroelectric (001)-oriented Bi_{0.9}La_{0.1}FeO₃ thin film. *Thin Solid Film.* **2022**, *754*, 139289. [[CrossRef](#)]
23. Yang, X.; Su, X.; Shen, M.; Zheng, F.; Xin, Y.; Zhang, L.; Hua, M.; Chen, Y.; Harris, V.G. Enhancement of Photocurrent in Ferroelectric Films Via the Incorporation of Narrow Bandgap Nanoparticles. *Adv. Mater.* **2012**, *24*, 1202–1208. [[CrossRef](#)]
24. Zhang, J.; Su, X.; Shen, M.; Dai, Z.; Zhang, L.; He, X.; Cheng, W.; Cao, M.; Zou, G. Enlarging photovoltaic effect: Combination of classic photoelectric and ferroelectric photovoltaic effects. *Sci. Rep.* **2013**, *3*, 2109. [[CrossRef](#)]
25. Xing, J.; Jin, K.-J.; Lu, H.; He, M.; Liu, G.; Qiu, J.; Yang, G. Photovoltaic effects and its oxygen content dependence in BaTiO_{3-δ}/Si heterojunctions. *Appl. Phys. Lett.* **2008**, *92*, 071113. [[CrossRef](#)]
26. Kamalasanan, M.N.; Chandra, S.; Joshi, P.C.; Mansingh, A. Structural and optical properties of sol-gel-processed BaTiO₃ ferroelectric thin films. *Appl. Phys. Lett.* **1991**, *59*, 3547–3549. [[CrossRef](#)]
27. Mondal, S.; Dutta, K.; Dutta, S.; Jana, D.; Kelly, A.G.; De, S. Efficient Flexible White-Light Photodetectors Based on BiFeO₃ Nanoparticles. *ACS Appl. Nano Mater.* **2018**, *1*, 625–631. [[CrossRef](#)]
28. Choi, T.; Lee, S.; Choi, Y.J.; Kiryukhin, V.; Cheong, S.W. Switchable Ferroelectric Diode and Photovoltaic Effect in BiFeO₃. *Science* **2009**, *324*, 63–66. [[CrossRef](#)]
29. Gao, R.; Fu, C.; Cai, W.; Chen, G.; Deng, X.; Cao, X. Thickness Dependence of Photovoltaic Effect in BiFeO₃ Thin Films Based on Asymmetric Structures. *J. Electron. Mater.* **2017**, *46*, 2373–2378. [[CrossRef](#)]

30. Gupta, S.; Tomar, M.; Gupta, V. Ferroelectric photovoltaic properties of Ce and Mn codoped BiFeO₃ thin film. *J. Appl. Phys.* **2014**, *115*. [[CrossRef](#)]
31. Inoue, R.; Ishikawa, S.; Imura, R.; Kitanaka, Y.; Oguchi, T.; Noguchi, Y.; Miyayama, M. Giant photovoltaic effect of ferroelectric domain walls in perovskite single crystals. *Sci. Rep.* **2015**, *5*, 14741. [[CrossRef](#)]
32. Han, F.; Zhang, Y.; Yuan, C.; Liu, X.; Zhu, B.; Liu, F.; Xu, J.; Zhou, C.; Wang, J.; Rao, G. Photocurrent and dielectric/ferroelectric properties of KNbO₃-BaFeO_{3-δ} ferroelectric semiconductors. *Ceram. Int.* **2020**, *46*, 14567–14572. [[CrossRef](#)]
33. Tian, M.; Liu, X.; Gong, A.; Zhang, S.; Wang, G.; Han, P.; Li, Y.; Lou, X.; Hao, X. Efficient ultraviolet-visible-near infrared self-powered photodetector based on hexagonal YMnO₃-based ferroelectric thin film by multiscale polarity structure optimization. *Chem. Eng. J.* **2023**, *452*, 139040. [[CrossRef](#)]
34. Zhang, Y.; Chen, J.; Cai, Y.; Zhang, Q.; Lu, Y.; Huang, H.; He, Y. Depolarization electric field and poling voltage-modulated Pb,La(Zr,Ti)O₃-based self-powered ultraviolet photodetectors. *J. Am. Ceram. Soc.* **2020**, *104*, 928–935. [[CrossRef](#)]
35. Cai, W.; Fu, C.; Gao, R.; Jiang, W.; Deng, X.; Chen, G. Photovoltaic enhancement based on improvement of ferroelectric property and band gap in Ti-doped bismuth ferrite thin films. *J. Alloys Compd.* **2014**, *617*, 240–246. [[CrossRef](#)]
36. Zhao, R.; Ma, N.; Song, K.; Yang, Y. Boosting Photocurrent via Heating BiFeO₃ Materials for Enhanced Self-Powered UV Photodetectors. *Adv. Funct. Mater.* **2019**, *30*, 1906232. [[CrossRef](#)]
37. Qi, J.; Ma, N.; Ma, X.; Adelung, R.; Yang, Y. Enhanced Photocurrent in BiFeO₃ Materials by Coupling Temperature and Thermo-Phototronic Effects for Self-Powered Ultraviolet Photodetector System. *ACS Appl. Mater. Interfaces* **2018**, *10*, 13712–13719. [[CrossRef](#)]
38. Matsuo, H.; Noguchi, Y.; Miyayama, M. Gap-state engineering of visible-light-active ferroelectrics for photovoltaic applications. *Nat. Commun.* **2017**, *8*, 207. [[CrossRef](#)]
39. Wang, L.; Ma, H.; Chang, L.; Ma, C.; Yuan, G.; Wang, J.; Wu, T. Ferroelectric BiFeO₃ as an Oxide Dye in Highly Tunable Mesoporous All-Oxide Photovoltaic Heterojunctions. *Small* **2017**, *13*, 1602355. [[CrossRef](#)]
40. Hua, H.; Bao, G.; Li, C.; Zhu, Y.; Yang, J.; Li, X. Effect of Ho, Mn co-doping on the structural, optical and ferroelectric properties of BiFeO₃ nanoparticles. *J. Mater. Sci. Mater. Electron.* **2017**, *28*, 17283–17287. [[CrossRef](#)]
41. Zhu, X.; Shi, P.; Kang, R.; Li, S.; Wang, Z.; Qiao, W.; Zhang, X.; He, L.; Liu, Q.; Lou, X. Enhanced energy storage density of Sr_{0.7}Bi_xTiO₃ lead-free relaxor ceramics via A-site defect and grain size tuning. *Chem. Eng. J.* **2021**, *420*, 129808. [[CrossRef](#)]
42. Luo, C.; Feng, Q.; Luo, N.; Yuan, C.; Zhou, C.; Wei, Y.; Fujita, T.; Xu, J.; Chen, G. Effect of Ca²⁺/Hf⁴⁺ modification at A/B sites on energy-storage density of Bi_{0.47}Na_{0.47}Ba_{0.06}TiO₃ ceramics. *Chem. Eng. J.* **2021**, *420*, 129861. [[CrossRef](#)]
43. Zhang, G.; Wu, H.; Li, G.; Huang, Q.; Yang, C.; Huang, F.; Liao, F.; Lin, J. New high T_c multiferroics KBiFe₂O₅ with narrow band gap and promising photovoltaic effect. *Sci. Rep.* **2013**, *3*, 1265. [[CrossRef](#)] [[PubMed](#)]
44. Cui, X.; Li, Y.; Li, X.; Hao, X. Enhanced photovoltaic effect in Bi₂FeMo_{0.7}Ni_{0.3}O₆ ferroelectric thin films by tuning the thickness. *J. Mater. Chem. C* **2020**, *8*, 1359–1365. [[CrossRef](#)]
45. Yang, L.; Wang, X.; Bai, L.; Xu, L.; Yang, Y. Boosted Photocurrent via Heating BiFeO₃ Thin Film for UV Photodetector at Wide Temperature Range. *Adv. Funct. Mater.* **2023**, *33*, 2303408. [[CrossRef](#)]
46. Qi, J.; Ma, N.; Yang, Y. Photovoltaic-Pyroelectric Coupled Effect Based Nanogenerators for Self-Powered Photodetector System. *Adv. Mater. Interfaces* **2017**, *5*, 1701189. [[CrossRef](#)]
47. Kathirvel, A.; Uma Maheswari, A.; Batabyal, S.K.; Sivakumar, M. BiFeO₃-Thiourea/Carbon heterostructure based self-powered white light photodetector. *Mater. Lett.* **2021**, *284*, 128906. [[CrossRef](#)]
48. Swain, A.B.; Rath, M.; Biswas, P.P.; Rao, M.S.R.; Murugavel, P. Polarization controlled photovoltaic and self-powered photodetector characteristics in Pb-free ferroelectric thin film. *APL Mater.* **2019**, *7*, 011106. [[CrossRef](#)]
49. Wu, M.; Jiang, Z.; Lou, X.; Zhang, F.; Song, D.; Ning, S.; Guo, M.; Pennycook, S.J.; Dai, J.; Wen, Z. Flexoelectric Thin-Film Photodetectors. *Nano Lett.* **2021**, *21*, 2946–2952. [[CrossRef](#)]
50. Tian, J.; Ma, S.; Xia, F.; Wang, Z.; Zhang, Y.; Dong, L. An efficient broadband white-light photodetector: Combining visible-light-active ferroelectrics with 2D conductive intermediary RGO. *Diam. Relat. Mater.* **2022**, *130*, 109449. [[CrossRef](#)]
51. Zheng, Z.; Gan, L.; Zhang, J.; Zhuge, F.; Zhai, T. An Enhanced UV-Vis-NIR and Flexible Photodetector Based on Electrospun ZnO Nanowire Array/PbS Quantum Dots Film Heterostructure. *Adv. Sci.* **2016**, *4*, 1600316. [[CrossRef](#)] [[PubMed](#)]
52. Wu, J.; Zhang, Y.; Yang, S.; Chen, Z.; Zhu, W. Thin MAPb_{0.5}Sn_{0.5}I₃ Perovskite Single Crystals for Sensitive Infrared Light Detection. *Front. Chem.* **2022**, *9*, 821699. [[CrossRef](#)] [[PubMed](#)]
53. Ma, S.; Xia, F.; Jia, R.; Sha, Z.; Tian, J.; Yu, L.; Dong, L. Discovery of a novel visible-light-active photodetector based on bismuth ferrite: Constructing and optimizing the Cr-doped-BiFeO₃/NiO thin film heterostructure. *Mater. Today Chem.* **2023**, *27*, 101309. [[CrossRef](#)]

Disclaimer/Publisher's Note: The statements, opinions and data contained in all publications are solely those of the individual author(s) and contributor(s) and not of MDPI and/or the editor(s). MDPI and/or the editor(s) disclaim responsibility for any injury to people or property resulting from any ideas, methods, instructions or products referred to in the content.